PASSIVE GRAVITY GRADIENT CAPTURE FOR IN-SPACE ASSEMBLY AND MANUFACTURING

Harsh G. Bhundiya[*], Zachary C. Cordero[†], and Michael A. Marshall[‡]

In-space assembly and manufacturing (ISAM) offers an opportunity to overcome the volume limitations of the rocket fairing and construct large structures optimized for loads in space. A key challenge for the design of ISAM spacecraft is the design of the attitude control system, which is complicated by the varying mass properties and environmental disturbances over long timescales of construction. In addition, it is unclear how disturbances such as gravity gradients can be advantageously used to minimize attitude control requirements. In this paper, we explore the strategy of gravity gradient capture, which refers to planning a passive attitude trajectory that results in a stable orientation after construction. We illustrate the concept with two case studies on the construction of truss structures—a 2D triangle unit cell and a 3D curved gridshell—by spacecraft in circular orbits. Based on the time reversibility of the equations of motion, we compute initial conditions that result in gravity gradient capture by solving the equations backward in time, considering the changes in mass properties from the prescribed construction sequence. Our analysis shows the feasibility of passive gravity gradient capture and the sensitivity of initial conditions to perturbations, which motivates future work on optimal attitude trajectories for ISAM spacecraft.

INTRODUCTION

The on-orbit construction of support structures, i.e., in-space assembly and manufacturing (ISAM), can dramatically enhance the performance of modern space systems for applications such as astronomy, communications, and remote sensing. The construction of truss support structures, in particular, has been of interest for supporting large space telescopes,[1] mesh reflector antennas,[2] and for enabling novel applications like space-based solar power.[3] For such applications, ISAM overcomes the limitations of the rocket fairing, enabling the construction of structures optimized for in-space loads with apertures larger than currently feasible with modern deployable technologies.[4,5] Numerous concepts for ISAM of truss support structures are currently under development, from robotic assembly of trusses,[6–8] extrusion of carbon fiber-reinforced thermoplastic trusses,[9–11] and deformation processing of trusses from ductile feedstock.[12]

An important challenge for the on-orbit construction of large structures is the design of the attitude control system (ACS) for ISAM spacecraft. Typically, ACSs are designed to reject environmental disturbance torques such as atmospheric drag, solar radiation pressure, and gravity gradients.[13] However, for ISAM missions, the ACS design is complicated by the varying mass properties and disturbance torques over the long fabrication timescales. For the construction of large truss structures, our previous analysis[14] has shown that maintaining a fixed orientation with limited attitude control authority results in fabrication times between months and years for 200-m diameter structures. Over such long timescales, the effects of the environmental disturbances on spacecraft attitude dynamics are coupled with the mass property changes, posing challenges to robust ACS design.

[*]Ph.D. Candidate, Department of Aeronautics and Astronautics, Massachusetts Institute of Technology, 77 Massachusetts Ave., Cambridge, MA 02139

[†]Esther and Harold E. Edgerton Associate Professor, Department of Aeronautics and Astronautics, Massachusetts Institute of Technology, 77 Massachusetts Ave., Cambridge, MA 02139

[‡]Guidance and Control Analyst, Space Exploration Sector, The Johns Hopkins University Applied Physics Laboratory, 11100 Johns Hopkins Rd., Laurel, MD 20723

At the same time, environmental disturbances provide opportunities for passive attitude control and stabilization. For example, gravity gradients have historically been used to stabilize long, "skinny" satellites such as the NASA Long Duration Exposure Facility.[15,16] Similarly, large spacecraft such as the International Space Station routinely use disturbance torques to minimize attitude control requirements. Two common approaches involve orienting the spacecraft to torque equilibrium attitudes which equilibrate multiple disturbance torques[17] and planning slew maneuvers with disturbance torques to avoid saturation of momentum actuators.[18] For ISAM spacecraft which undergo changes in mass properties over long timescales, it is currently unclear how environmental disturbances such as gravity gradients can be advantageously used to minimize attitude control.

In this paper, we explore the feasibility of a passive attitude control strategy for ISAM spacecraft that relies on the coupled effects of changes in mass properties and gravity gradients. The approach, referred to as passive gravity gradient capture, plans a passive attitude trajectory during ISAM such that the final orientation remains stable in the presence of gravity gradients, as illustrated in Fig. 1. The benefits of this approach are that there is no requirement for attitude control during the construction sequence itself, and there is no tumbling after the the construction is complete. Passive gravity gradient capture has been previously demonstrated, e.g., for the deployment of booms on the Radio Astronomy Explorer spacecraft launched in 1968 and 1973.[19–21] These spacecraft consisted of four 200-m long deployable antenna booms arranged in a cruciform geometry and two additional 100-m long damper booms. A rigid body dynamics model was used to optimize the timing of boom deployment in multiple phases to achieve passive attitude trajectories with stable pitch oscillations after deployment.[19] These missions successfully demonstrated the feasibility of gravity gradient capture for boom deployment, but the concept remains largely unexplored in the context of ISAM. To that end, the objective of this paper is to understand the feasibility of passive gravity gradient capture for ISAM through case studies involving the construction of truss support structures.

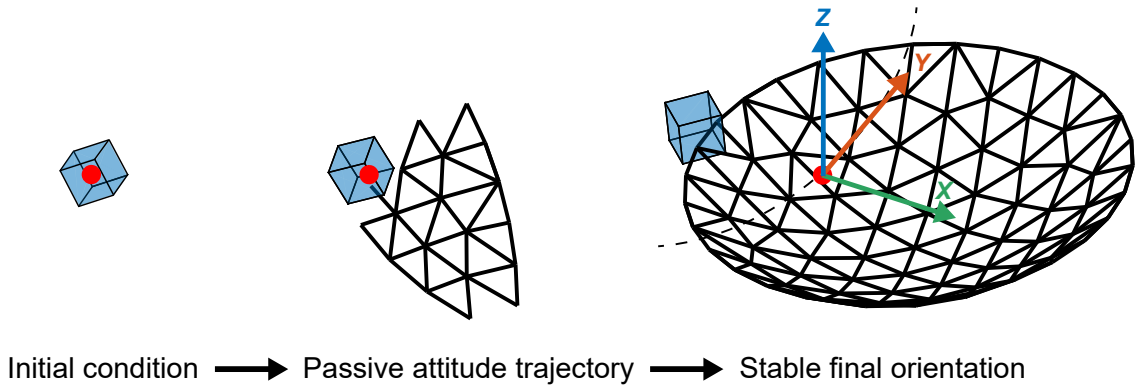

Figure 1: Gravity gradient capture for ISAM spacecraft: a passive attitude trajectory from a specific initial condition yields a stable final orientation after the construction process.

MOTIVATING EXAMPLE

We begin with a motivating example to illustrate the importance of environmental disturbance torques on the attitude dynamics of ISAM spacecraft. Consider a simplified model of a thin cylindrical disk with constant density ρ, constant height-to-diameter ratio $\epsilon \ll 1$, and a time-varying diameter $D(t)$ (Fig. 2). As a first approximation, an increase in the diameter of the disk models the deployment or construction of an antenna aperture in space.

We are interested in a scaling analysis to understand the angular accelerations of the disk from its varying mass properties and environmental disturbances in orbit. To this end, we derive scaling relations for the magnitudes of angular acceleration as a function of disk diameter and diameter growth rate, following a methodology similar to a previous length scaling analysis.[22] An important difference in the present analysis

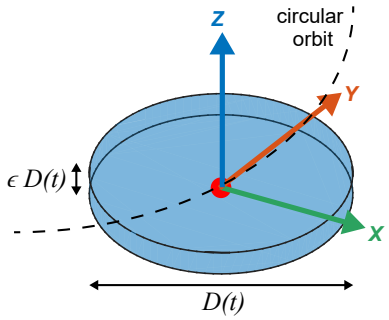

Figure 2: Thin, circular disk with varying diameter $D(t)$

is the additional torque from the diameter growth rate used to represent the construction rate for the ISAM process.

We model the attitude dynamics of the disk in a circular orbit using the Newton-Euler equations of motion for a rigid body,[13]

$$[\boldsymbol{I}_{CM}]\dot{\boldsymbol{\omega}} + \boldsymbol{\omega} \times [\boldsymbol{I}_{CM}]\boldsymbol{\omega} = \boldsymbol{\tau}_{\text{MD}} + \boldsymbol{\tau}_{\text{GG}} + \boldsymbol{\tau}_{\text{AD}} + \boldsymbol{\tau}_{\text{SP}} \tag{1}$$

Here, dot notation denotes differentiation with respect to time t, $\boldsymbol{\omega}$ is the angular velocity of the disk with respect to an inertial frame, and $[\boldsymbol{I}_{CM}]$ is the time-varying mass moment of inertia about its center of mass,

$$[\boldsymbol{I}_{CM}] = \frac{\pi}{32}\rho\epsilon D(t)^5 \begin{bmatrix} \frac{1}{6}\left(3+4\epsilon^2\right) & & \\ & \frac{1}{6}\left(3+4\epsilon^2\right) & \\ & & 1 \end{bmatrix}. \tag{2}$$

The terms on the right-hand side of Eq. 1 represent the torques from the varying mass distribution (MD) and environmental disturbances due to gravity gradients (GG), atmospheric drag (AD), and solar radiation pressure (SP). The torque from the time rate of change in disk inertia is given by[23]

$$\boldsymbol{\tau}_{\text{MD}} = -[\dot{\boldsymbol{I}}_{CM}]\boldsymbol{\omega}. \tag{3}$$

The gravity gradient torque, which results from variations in the gravitational force at different points on the body, is modeled as[13]

$$\boldsymbol{\tau}_{\text{GG}} = 3n^2(\hat{\boldsymbol{R}}_{CM} \times [\boldsymbol{I}_{CM}]\hat{\boldsymbol{R}}_{CM}), \tag{4}$$

where $n = 2\pi/T$ is the angular velocity of a circular orbit with period T, and $\hat{\boldsymbol{R}}_{CM}$ is the unit vector pointing from the center of the Earth to the center of mass of the spacecraft. The other two disturbances result from collisions with atmospheric particles and photons from solar flux, imparting atmospheric drag and solar radiation pressure on the disk. These disturbances apply forces to the spacecraft, and if the center of pressure is offset from the center of mass, torques of the form

$$\boldsymbol{\tau} = \boldsymbol{\delta} \times \boldsymbol{F}, \tag{5}$$

where $\boldsymbol{\delta}$ is the vector from the center of mass to the center of pressure and $\boldsymbol{F}$ is the disturbance force. The disturbance forces due to atmospheric drag and solar radiation pressure are[13]

$$\boldsymbol{F}_{\text{AD}} = -\frac{1}{2}\rho_A C_D A_C v^2 \hat{\boldsymbol{v}}, \tag{6}$$

$$\boldsymbol{F}_{\text{SP}} = 2PA_C \cos^2\gamma_s \hat{\boldsymbol{n}}, \tag{7}$$

where ρ_A is the atmospheric density at the orbit altitude, C_D is the drag coefficient, A_C is the cross-sectional area of the disk normal to the velocity vector, $\boldsymbol{v}$ is the orbital velocity vector with magnitude v and direction

$\hat{\boldsymbol{v}}$, P is the effective solar radiation pressure, γ_s is the angle between the surface normal and the Sun, and $\hat{\boldsymbol{n}}$ is the surface normal vector. For simplicity, Eq. 6 does not account for the rotation rate of Earth's atmosphere.

To derive scaling relations for the angular accelerations due to these disturbance torques, we make several simplifying assumptions similar to the previous analysis.[22] First, we assume that the disk spins slowly such that its angular velocity is approximately equal to the orbit angular velocity, i.e., $||\boldsymbol{\omega}||_2 \approx n$. This is a reasonable assumption for nadir-pointing spacecraft and simplifies Eq. 1 such that the angular acceleration $\alpha \equiv \dot{\omega}$ is proportional to the moment of inertia, i.e.,

$$\alpha = \frac{\tau}{I}. \tag{8}$$

Next, we assume that the offset vector $\boldsymbol{\delta}$ remains in the plane of the disk (due to the small thickness of the disk) and that its magnitude is proportional to the disk's diameter, i.e., $\delta = \kappa_T D(t)$ where κ_T is a scale factor. A scale factor of $\kappa_T = 0.01$ represents a moment arm that is 1% of the diameter of the disk. To estimate the maximum angular accelerations from the atmospheric drag and solar radiation pressure, we then consider the case where the cross-sectional area of the disk is perpendicular to the orbital velocity and the Sun vector. Finally, for the gravity gradient disturbance, we consider orientations that yield the maximum torque. With these assumptions, the magnitudes of the angular accelerations due to these disturbance torques are

$$\alpha_{\text{MD}} = 5n\dot{D}D^{-1}, \tag{9}$$

$$\alpha_{\text{GG}} = \frac{3n^2(3-4\epsilon^2)}{2(3+4\epsilon^2)}, \tag{10}$$

$$\alpha_{\text{AD}} = \frac{48\rho_A\kappa_T(n\mu_E)^{2/3}}{\rho\epsilon(3+4\epsilon^2)}D^{-2}, \tag{11}$$

$$\alpha_{\text{SP}} = \frac{96\kappa_T P}{\rho\epsilon(3+4\epsilon^2)}D^{-2}. \tag{12}$$

Equations 9–12 demonstrate that the angular acceleration from the rate of change of inertia (MD) scales with the ratio of the diameter growth rate to the instantaneous diameter. In contrast, the angular acceleration due to gravity gradients (GG) is independent of size and scales only with n^2, whereas the angular accelerations due to atmospheric drag (AD) and solar pressure (SP) scale with D^{-2}. To understand the relative magnitudes of the angular accelerations, Fig. 3 plots Eqs. 9–12 as a function of the disk's diameter for three different orbit regimes, with the parameters listed in Table 1. In Table 1, LEO, MEO, and GEO denote low Earth orbit, medium Earth orbit, and geosynchronous Earth orbit, respectively. The figures plot α_{MD} for two different constant diameter growth rates: $\dot{D} = 10^{-1}$ m/s is representative of the deployment of reflector antennas that achieve diameters of up to 25 m in minutes,[2] whereas $\dot{D} = 10^{-3}$ m/s is representative of a slower construction process such as the extrusion of composite feedstock.[9]

Parameter	**Value**
ϵ	0.1
κ_T	0.01
ρ	79 kg/m^3
ρ_A (LEO)	6.97×10^{-13} kg/m^3
ρ_A (MEO)	7.86×10^{-30} kg/m^3
ρ_A (GEO)	1.29×10^{-71} kg/m^3
μ_E	3.986×10^{14} m^3/s^2
P	4.56×10^{-6} N/m^2

Table 1: Disk and environmental disturbance parameters

Figure 3 shows that for faster diameter growth rates ($\dot{D} = 10^{-1}$ m/s), the largest angular acceleration at all orbit altitudes results from the rate of inertia change, with negligible effects due to environmental disturbances. On the other hand, for slower diameter growth rates ($\dot{D} = 10^{-3}$ m/s), the environmental disturbances

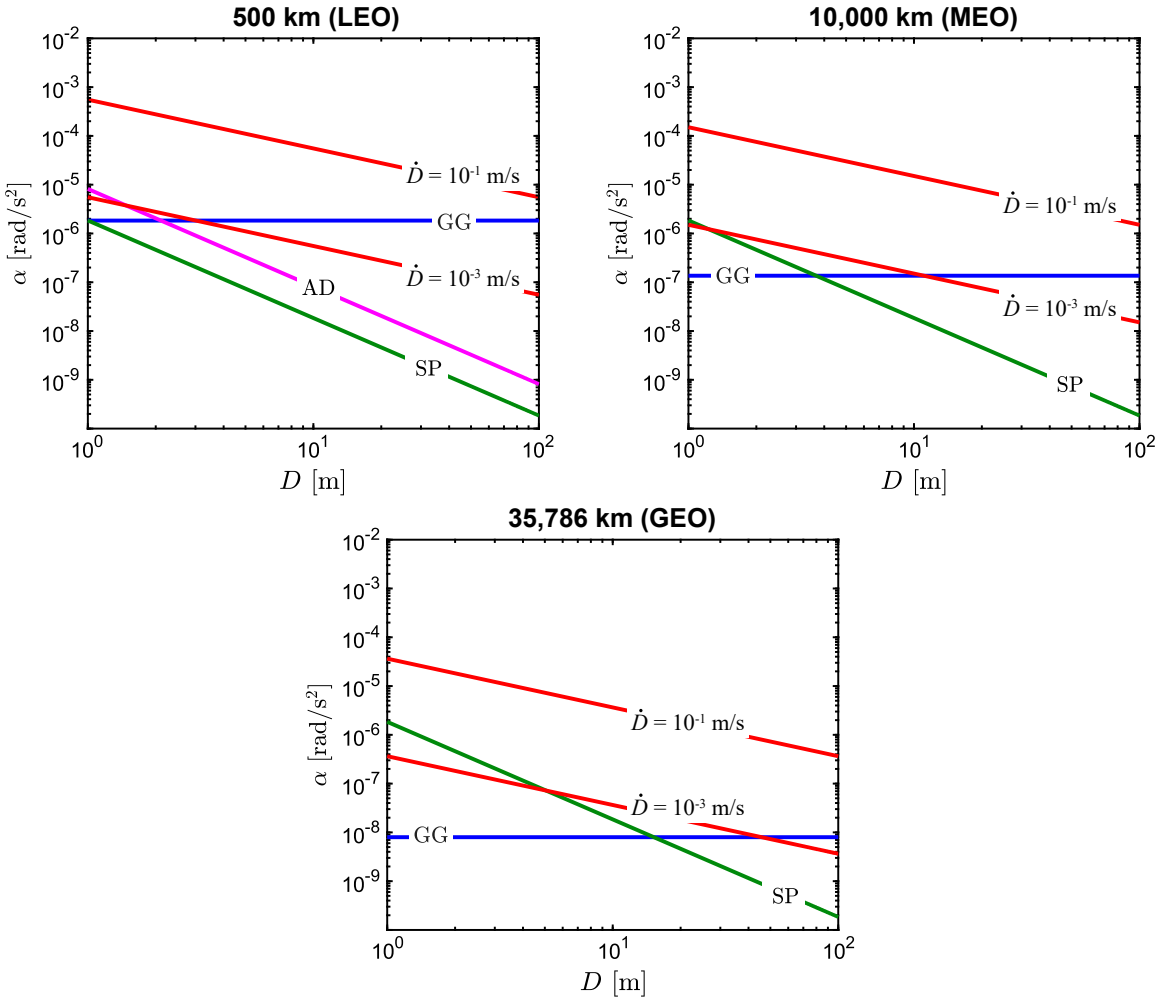

Figure 3: Angular accelerations as a function of disk diameter for different orbit regimes: low Earth orbit (500 km), medium Earth orbit (10,000 km), and geostationary orbit (35,786 km).

are the dominant contributors to the attitude dynamics at some diameter scales. In LEO, atmospheric drag dominates for smaller diameters ($D < 5$ m), whereas the gravity gradient dominates for larger diameters. Likewise, in MEO and GEO, solar radiation pressure and gravity gradients are dominant. As the diameter growth rate decreases further ($\dot{D} \ll 10^{-3}$ m/s), the environmental disturbances increasingly dominate the attitude dynamics. Taken together, this scaling analysis demonstrates the importance of understanding the coupled effects of mass property changes and environmental disturbances on the attitude dynamics of ISAM spacecraft, particularly for slower construction rates.

PASSIVE GRAVITY GRADIENT CAPTURE

The scaling analysis in the previous section has shown that gravity gradients are length independent and dominate the environmental disturbances in LEO for large diameters ($D > 5$ m) and slow diameter growth rates ($\dot{D} = 10^{-3}$ m/s). For real truss structures, the cross-sectional area of sparsely distributed struts is also much smaller than that of a solid disk, reducing the relative effects of atmospheric drag and solar radiation pressure. Hence, we focus our attention on the effects of gravity gradients and study how changes in mass properties and gravity gradients affect the attitude dynamics of ISAM spacecraft.

We specifically model the spacecraft and fabricated structure as a single combined control volume with

relative motion and mass redistribution from the construction process. Assuming a circular orbit with angular velocity $n = 2\pi/T$ and period T, the non-dimensional equations of motion of the variable-mass system are[24,25]

$$\dot{\boldsymbol{q}} = \pi \boldsymbol{\Omega}(\hat{\boldsymbol{\omega}})\boldsymbol{q}, \tag{13}$$

$$\dot{\hat{\boldsymbol{\omega}}} = -2\pi[\boldsymbol{I}_{CM}]^{-1}\left(\hat{\boldsymbol{\omega}} \times [\boldsymbol{I}_{CM}]\hat{\boldsymbol{\omega}}\right) + \hat{\boldsymbol{\alpha}}_{\text{MD}} + \hat{\boldsymbol{\alpha}}_{\text{GG}}. \tag{14}$$

where dot notation denotes derivatives with respect to non-dimensional time $\hat{t} = t/T$. In Eq. 13, $\boldsymbol{q}$ is the unit quaternion describing the orientation of the body frame with respect to the inertial frame and $\boldsymbol{\Omega}(\hat{\boldsymbol{\omega}})$ is the operator[24]

$$\boldsymbol{\Omega}(\hat{\boldsymbol{\omega}}) \triangleq \begin{bmatrix} 0 & -\hat{\omega}_x & -\hat{\omega}_y & -\hat{\omega}_z \\ \hat{\omega}_x & 0 & \hat{\omega}_z & -\hat{\omega}_y \\ \hat{\omega}_y & -\hat{\omega}_z & 0 & \hat{\omega}_x \\ \hat{\omega}_z & \hat{\omega}_y & -\hat{\omega}_x & 0 \end{bmatrix}. \tag{15}$$

The terms in Eq. (14) are expressed in the body-fixed frame. Specifically, $\hat{\boldsymbol{\omega}} = \boldsymbol{\omega}/n$ is the non-dimensional angular velocity of the body frame with respect to the inertial frame and $[\boldsymbol{I}_{CM}(\hat{t})]$ is the time-varying moment of inertia matrix about the instantaneous center of mass. Additionally, $\hat{\boldsymbol{\alpha}}_{\text{MD}}$ and $\hat{\boldsymbol{\alpha}}_{\text{GG}}$ are the non-dimensional angular accelerations from the varying mass properties and the gravity gradient torque, given by[25,26]

$$\hat{\boldsymbol{\alpha}}_{\text{MD}} = -[\boldsymbol{I}_{CM}]^{-1}\left([\dot{\boldsymbol{I}_{CM}}]\hat{\boldsymbol{\omega}} + \hat{\boldsymbol{\omega}} \times \boldsymbol{h}_{CM} + \frac{\dot{\boldsymbol{h}}_{CM}}{2\pi}\right), \tag{16}$$

$$\hat{\boldsymbol{\alpha}}_{\text{GG}} = 6\pi[\boldsymbol{I}_{CM}]^{-1}\left(\hat{\boldsymbol{R}}_{CM} \times [\boldsymbol{I}_{CM}]\hat{\boldsymbol{R}}_{CM}\right), \tag{17}$$

$$\tag{18}$$

where

$$\boldsymbol{h}_{CM} = \sum_{i=1}^{N} m_i(\boldsymbol{r}_i - \boldsymbol{r}_{CM}) \times (\dot{\boldsymbol{r}}_i - \dot{\boldsymbol{r}}_{CM}) \tag{19}$$

is the angular momentum of the bodies inside the control volume relative to the instantaneous center of mass, and $\hat{\boldsymbol{R}}_{CM}$ is the unit vector pointing from the orbit center to the instantaneous center of mass. The angular momentum is a function of the positions $\boldsymbol{r}_i$ of an arbitrary number of point masses m_i within the control volume and the position $\boldsymbol{r}_{CM}$ of the instantaneous center of mass. For a construction process that sequentially extrudes struts to fabricate truss structures, each point mass m_i represents a strut that moves relative to the spacecraft.

Together, Eqs. 13–19 govern the attitude dynamics of an ISAM spacecraft with angular accelerations from both the changes in mass distribution ($\hat{\boldsymbol{\alpha}}_{\text{MD}}$) and the gravity gradient disturbance ($\hat{\boldsymbol{\alpha}}_{\text{GG}}$). We are interested in modeling the attitude dynamics of ISAM spacecraft during long construction timescales and understanding how gravity gradients can be used advantageously to reduce the required torque and angular momentum storage for the ACS. Importantly, Eqs. 13–19 are invariant under the change of variables $\left(\hat{t}, \hat{\boldsymbol{\omega}}\right) \rightarrow -\left(\hat{t}, \hat{\boldsymbol{\omega}}\right)$. This implies that the system is *time reversible*, i.e., its trajectories are symmetric forward and backward in time.[27]

Time reversibility provides a computational tool for assessing the feasibility of passive gravity gradient capture. There are multiple equilibrium orientations where the principal inertia axes are aligned with the local-vertical-local-horizontal (LVLH) orbit frame such that there are no gravity gradient torques on a spacecraft.[15,28] Moreover, gravity gradients provide a stabilizing restoring torque when the minimum principal inertia axis is aligned with the orbit radius vector.[26] As a result, if an ISAM spacecraft can be passively maneuvered into this final orientation solely from the changes in mass distribution and gravity gradients, active attitude control is unnecessary during the construction process. In what follows, we present two case studies that demonstrate the feasibility of gravity gradient capture for two relevant truss structures.

TRIANGLE UNIT CELL

We first demonstrate passive gravity gradient capture for the construction of a 2D equilateral triangle in the orbit plane (Fig. 4). We assume a spacecraft in circular orbit sequentially extruding struts, a construction approach that is representative of many of the candidate ISAM processes for truss structures.[7,8,12] The equilateral triangle is relevant as a unit cell for larger truss structures such as the curved gridshell studied in the next section.

For this 2D geometry, the motion is restricted to the orbit plane. As a result, the moment equilibrium of Eq. 14 simplifies because the only relevant rotation is the pitch θ_z about the orbit-normal axis,

$$\ddot{\theta}_z = 3\pi \left(\frac{I_{xx} - I_{yy}}{I_{zz}} \right) \sin\left(2\theta_z\right) + 6\pi \left(\frac{I_{xy}}{I_{zz}} \right) \cos\left(2\theta_z\right) - \left(\frac{\dot{I}_{zz}}{I_{zz}} \right) \left(\dot{\theta}_z + 1 \right) - \frac{1}{2\pi} \left(\frac{\dot{h}_z}{I_{zz}} \right). \tag{20}$$

The first two terms of Eq. 20 correspond to the angular accelerations from the gravity gradients, and the last two terms correspond to the rate of change in the mass distribution. The moments of inertia I_{xx}, I_{yy}, and I_{xy} are the time-varying components of the moment of inertia matrix about the instantaneous center of mass,

$$[\boldsymbol{I}_{CM}] = \begin{bmatrix} I_{xx}(\hat{t}) & I_{xy}(\hat{t}) & \\ I_{xy}(\hat{t}) & I_{yy}(\hat{t}) & \\ & & I_{zz}(\hat{t}) \end{bmatrix}, \tag{21}$$

and h_z is the non-zero component of the angular momentum from the relative motion of the struts and spacecraft relative to the center of mass (Eq. 19). Since there are no external forces on the body (besides gravity), the instantaneous center of mass remains on the circular orbit.

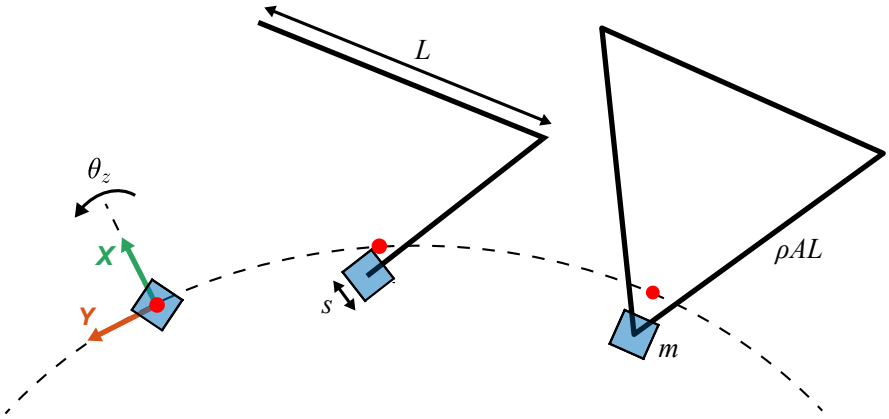

Figure 4: Construction of a 2D triangle unit cell in the orbit plane. Gravity gradient capture is achieved when the triangle faces radially inwards or outwards, i.e., $\theta_z = 0$ or $\theta_z = \pi$.

To compute the change in mass distribution during construction, we consider a cubic spacecraft with side length s and mass m_{SC} sequentially extruding three struts of length L and linear density ρA to construct an equilateral triangle. We model each strut as a slender rod of varying mass and length, with a smooth extrusion profile with zero velocity, acceleration, and jerk at the end points.[14] The extrusion of all three struts occurs during the period $\hat{t} \in [0, \hat{t}_F]$, where $\hat{t}_F$ represents the construction timescale in number of orbits. After the three struts have been extruded, the final moment of inertia matrix of the truss and spacecraft about their respective centers of mass are:

$$[\boldsymbol{I}_T] = \frac{1}{4}\rho A L^3 \begin{bmatrix} 1 & & \\ & 1 & \\ & & 2 \end{bmatrix}, \tag{22}$$

$$[\boldsymbol{I}_{SC}] = \frac{1}{6} m_{SC} s^2 \boldsymbol{I}_{3\times 3}, \tag{23}$$

where $\boldsymbol{I}_{3\times3}$ is an identity matrix. For this specific geometry, Eq. 20 can be further simplified using the final mass and inertia ratios between the truss and spacecraft,

$$\eta_M = \frac{3\rho AL}{m_{SC}}, \tag{24}$$

$$\eta_I = \left(\frac{3\rho AL}{m_{SC}}\right)\left(\frac{L}{s}\right)^2. \tag{25}$$

For given mass and inertia ratios (η_M, η_I) and a construction timescale $(\hat{t}_F)$, Eq. 20 can be numerically integrated to find the orientation of the during the construction of the triangle unit cell.

The final orientation that results in zero disturbance torque consists of the triangle facing radially inward or outward ($\theta_z = 0$ or $\theta_z = \pi$), as depicted in Fig. 4. To find attitude trajectories for passive gravity gradient capture, we use time reversibility to solve Eq. 20 backward in time from these final orientations. Numerically, this involves integrating from some final time $\hat{t}_F$ to time $\hat{t} = 0$ and specifying the time-varying mass distribution starting from the final configuration and ending in the initial configuration.

Figures 5 and 6 plot two representative trajectories for passive gravity gradient capture that both result in the final orientation $\theta_z = 0$. The figures plot the trajectories in the phase plane $(\theta_z, \dot{\theta}_z/n)$ with the pitch rate non-dimensionalized by the orbit angular velocity n. The first trajectory (Fig. 5) begins with a positive angular velocity that decreases monotonically to zero as the struts are extruded. This trajectory is dominated by the torques from the rate of change in inertia, i.e., the last two terms of Eq. 20, due to the high initial angular velocity of the spacecraft. The second trajectory (Fig. 6) begins with a negative angular velocity but reaches an equilibrium orientation with zero angular velocity after the extrusion of each strut. The gravity gradient torque has a larger effect on this trajectory and causes its angular velocity to change signs multiple times. Together, the trajectories demonstrate the feasibility of using the combined effects of the gravity gradients and the construction process to yield a desirable final orientation.

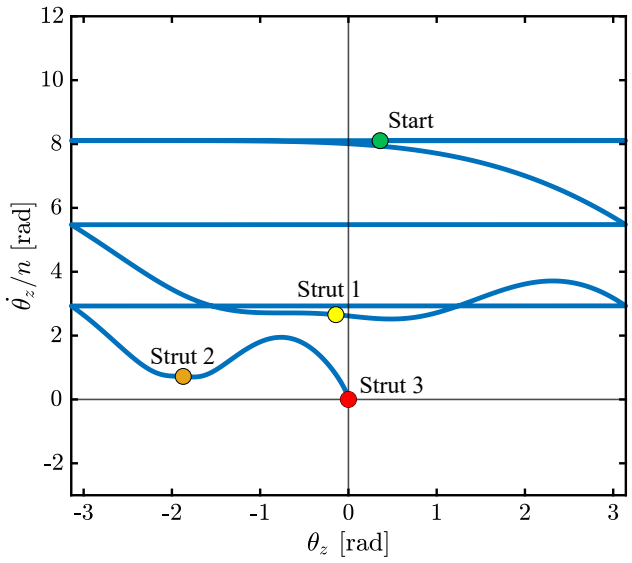

Figure 5: Passive trajectory for gravity gradient capture of the 2D triangle with $(\eta_M, \eta_I, \hat{t}_F) = (0.03, 2.5, 1)$.

Energy Criterion for 2D Gravity Gradient Capture

The passive trajectories of Figs. 5 and 6 achieve a perfect equilibrium orientation with zero disturbance torque at the end of construction. However, feasible trajectories for passive gravity gradient capture include any trajectory that results in a final state that remains stable in the presence of gravity gradient torques.

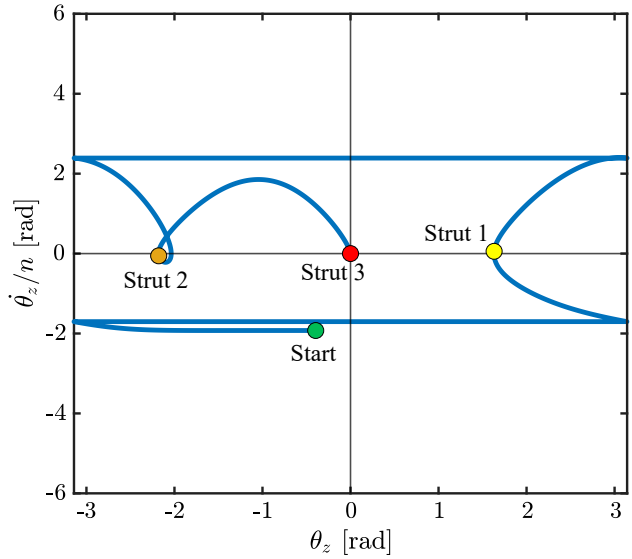

Figure 6: Passive trajectory for gravity gradient capture of the 2D triangle with $(\eta_M, \eta_I, \hat{t}_F) = (0.06, 10, 1.5)$.

For the 2D triangle unit cell, we can classify the stability of the final state by considering the total energy $H(\theta_z, \dot{\theta}_z)$ of the spacecraft after construction, which is the sum of its rotational kinetic and gravitational potential energies,[29]

$$H(\theta_z, \dot{\theta}_z) = \frac{1}{2} I_{zz}(\hat{t}_F)(\dot{\theta}_z n)^2 + \frac{3}{4} n^2 \left(\left(I_{xx}(\hat{t}_F) - I_{yy}(\hat{t}_F) \right) \cos(2\theta_z) - 2 I_{xy}(\hat{t}_F) \sin(2\theta_z) \right). \tag{26}$$

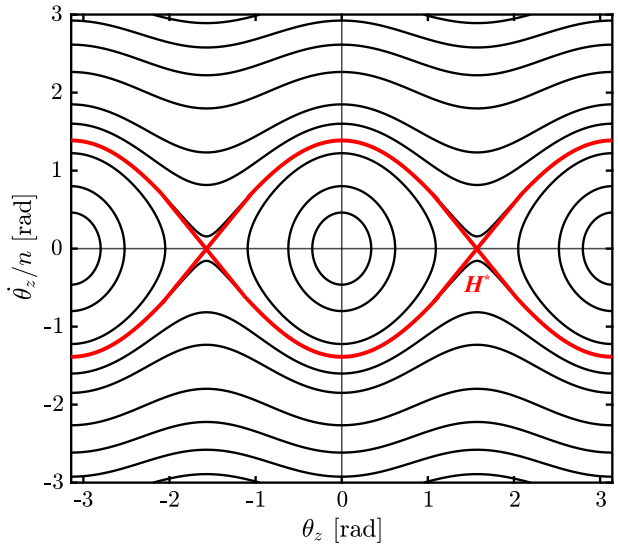

Figure 7: Contours of $H(\theta_z, \dot{\theta}_z)$ for trajectories with no change in mass distribution. The critical energy H^* corresponds to the transition between stable oscillations and complete revolutions, similar to a pendulum.

Figure 7 depicts contours of the total energy $H(\theta_z, \dot{\theta}_z)$ (Eq. (26)) in the phase plane. In the absence of mass redistribution, the gravity gradient torque causes the spacecraft to oscillate back and forth near the

equilibrium points $(\theta, \dot{\theta}_z) = (0, 0)$ and $(\theta, \dot{\theta}_z) = (\pi, 0)$, similar to a pendulum. As a result, 2D attitude trajectories conserve the total energy after construction, i.e., for $\hat{t} \geq \hat{t}_F$. Additionally, there is a critical energy H^*, below which the spacecraft experiences a stable oscillation about an equilibrium point, and above which it tumbles. This critical energy corresponds to the unstable equilibrium points $(\theta_z, \dot{\theta}_z) = (\pm\pi/2, 0)$ that separate the resonance islands, i.e.,

$$H^* = H(\pm\pi/2, 0) = -\frac{3}{4} n^2 \left(I_{xx}(\hat{t}_F) - I_{yy}(\hat{t}_F) \right). \tag{27}$$

Using Eq. (27), we can classify the final state of the spacecraft as stable if $H(\hat{t}_F) < H^*$ and unstable if $H(\hat{t}_F) \geq H^*$.

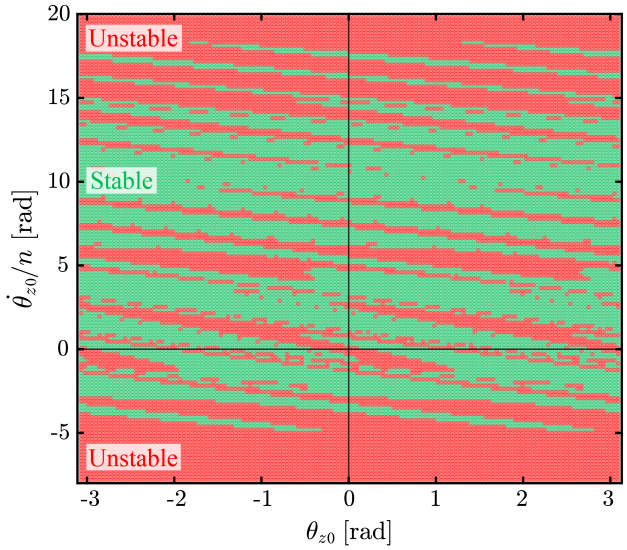

Figure 8: Range of initial conditions for gravity gradient capture of the 2D triangle with $(\eta_M, \eta_I, \hat{t}_F) = (0.03, 2.5, 1)$.

Using this energy criterion, we can determine the full range of initial conditions for passive gravity gradient capture of the 2D triangle unit cell, as depicted in Fig. 8 for $(\eta_M, \eta_I, \hat{t}_F) = (0.03, 2.5, 1)$. The green and red regions in Fig. 8 represent initial conditions that respectively result in stable and unstable final states. For initial angular velocities of $\dot{\theta}_{z0}/n > 18.5$ and $\dot{\theta}_{z0}/n < -5$, Fig. 8 shows that all initial conditions result in unstable final states. However, within this range, there is a wide range of possible initial conditions for gravity gradient capture, i.e., the green bands in the phase plane. The widths of the bands vary between $\Delta\dot{\theta}_{z0}/n \approx [0.5, 2]$, with wider bands near zero angular velocity. Here, the larger number of initial conditions with positive angular velocity is the result of the prograde circular orbit with positive angular velocity ($n > 0$) coupled with the fact that the increase in inertia during construction decreases the angular velocity. For a retrograde orbit ($n < 0$), the green regions are reflected about the horizontal axis.

Initial Condition Sensitivity

An important practical consideration for passive gravity gradient capture is the sensitivity of the final state to the corresponding initial conditions. To understand the sensitivity of the initial conditions for the 2D triangle unit cell, we consider the effect of a small initial tilt (ϕ) out of the orbit plane on the final state. The tilt angle ϕ represents a rotation about an axis parallel to the orbit plane such that the initial orientation is specified by the ZYX Euler angle sequence $(\theta_{z0}, \phi, 0)$ relative to the orbit frame (cf. Fig. 4).

Figures 9 and 10 plot representative trajectories for passive gravity gradient capture using the initial condition of Fig. 5 with the addition of initial tilt angles $\phi = 1^\circ$ and $\phi = 5^\circ$. By adding the initial tilt, the rotation

of the spacecraft is no longer restricted to the orbit plane; for this reason, these trajectories are solutions to the full 3D equations of motion (Eqs. 13–19). The figures plot the trajectories in the phase plane of the three Euler angles and the three angular velocity components in the body-fixed frame. With the smaller tilt angle $\phi = 1^\circ$, the trajectory is similar to the corresponding trajectory with zero tilt (Fig. 5), but the spacecraft experiences small oscillations in roll and yaw after strut extrusion. These oscillations are small enough that the final state remains near the equilibrium point and achieves gravity gradient capture. However, with the larger tilt angle $\phi = 5^\circ$, the initial angular velocity of the spacecraft causes the tilt angle to grow, resulting in a final state that is far from the desired equilibrium point.

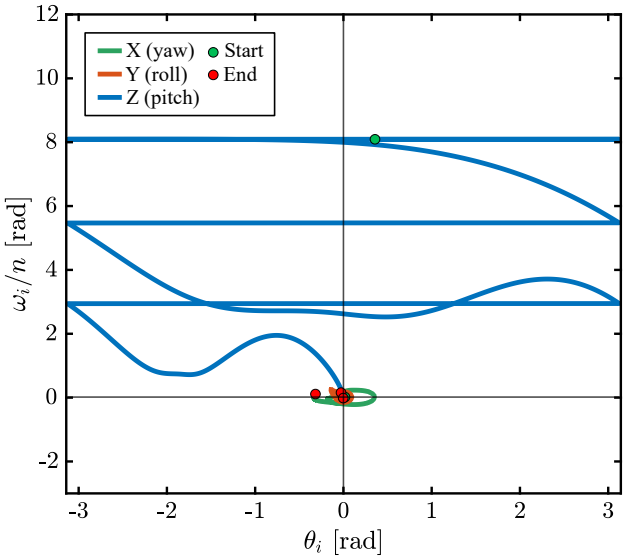

Figure 9: Passive trajectory for gravity gradient capture of the 2D triangle with an initial tilt of $\phi = 1^\circ$.

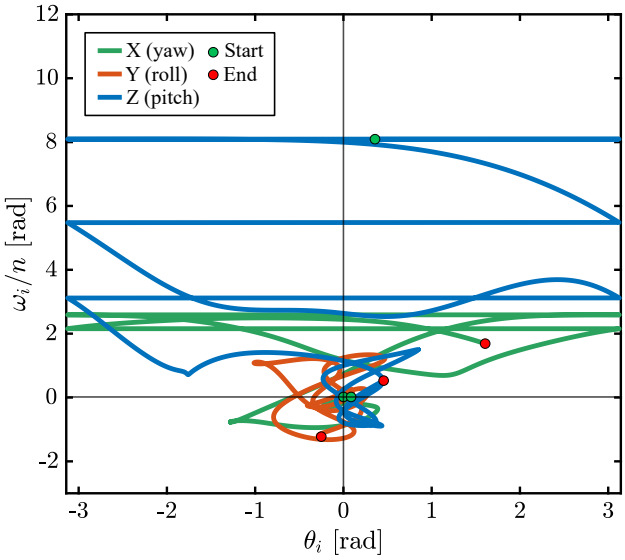

Figure 10: Passive trajectory for gravity gradient capture of the 2D triangle with an initial tilt of $\phi = 5^\circ$.

To classify the stability of the final state due to the initial conditions plus tilt, we linearize the equations of motion about the final state $\left(\boldsymbol{q}(\hat{t}_F), \hat{\boldsymbol{\omega}}(\hat{t}_F)\right)$. The nonlinear system is unstable if any eigenvalues of the

corresponding Jacobian matrix have positive real part, and are linearly stable otherwise.[27] Using this linear stability criterion, Figs. 11 and 12 plot the stability of the final states due to the range of initial conditions from Fig. 8 for $(\eta_M, \eta_I, \hat{t}_F) = (0.03, 2.5, 1)$ with the initial tilt angles $\phi = 1^\circ$ and $\phi = 5^\circ$. The smaller tilt angle $\phi = 1^\circ$ again has a minor effect on the range of stable initial conditions; however, the larger tilt angle $\phi = 5^\circ$ destabilizes many of the previously stable final states, only leaving stable initial conditions within a narrow angular velocity range $\Delta\dot{\theta}_{z0}/n \approx [-5, 5]$. Because the angular velocity is non-dimensionalized with respect to the orbit angular velocity, higher orbit altitudes are more sensitive to the initial tilt. Thus, even though the 2D triangle unit cell has a wide range of initial conditions that result in gravity gradient capture, the final states are sensitive to initial condition perturbations such as tilt out of the orbit plane.

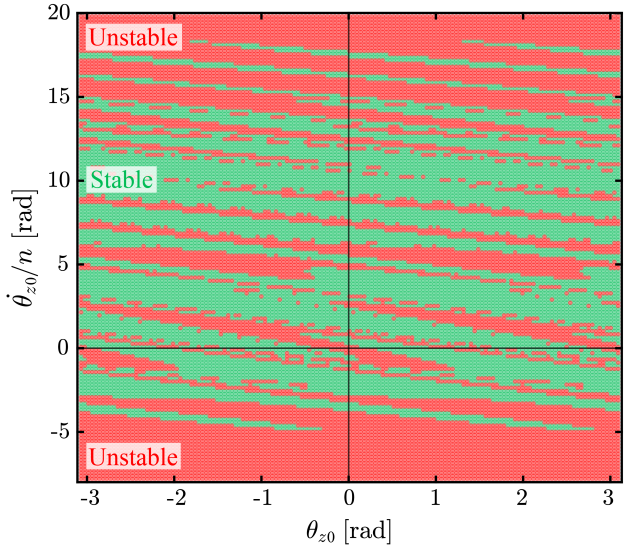

Figure 11: Range of initial conditions for passive gravity gradient capture of the 2D triangle with an initial tilt of $\phi = 1^\circ$.

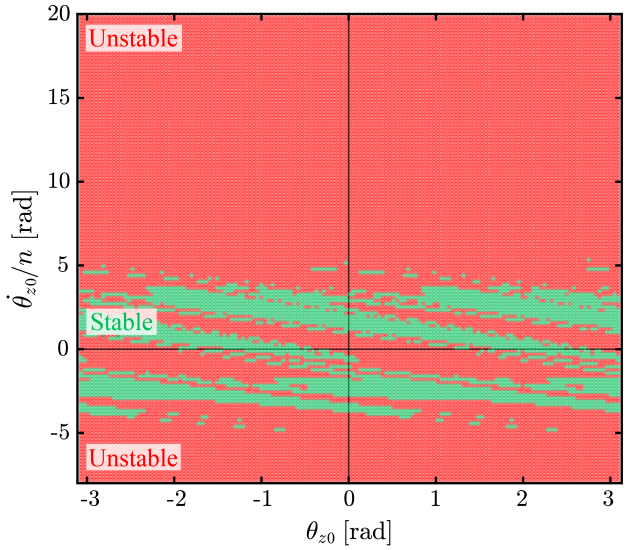

Figure 12: Range of initial conditions for passive gravity gradient capture of the 2D triangle with an initial tilt of $\phi = 5^\circ$.

CURVED GRIDSHELL

To understand the feasibility of gravity gradient capture for more complex truss geometries, we extend the above analysis to the gravity gradient capture of a 3D curved gridshell, an efficient support structure geometry for antennas and telescopes.[30] We again assume a spacecraft in circular orbit sequentially extruding struts to construct the gridshell.

To compute passive attitude trajectories for gravity gradient capture, we solve the 3D equations of motion (Eqs. 13–19) backward in time from a stable equilibrium orientation with zero gravity gradient torque, similar to the approach in 2D. For the gridshell, this stable orientation occurs when the principal inertia axes are aligned with the orbit frame such that $I_{xx} \leq I_{yy} \leq I_{zz}$,[15,28] as depicted in Fig. 1. Here, the gridshell has diameter D, focal length-to-diameter ratio F/D, average strut length L, strut linear density ρA, and total mass m_T after construction, and the cubic spacecraft has side length s and mass m_{SC} after construction. To specify the construction sequence, we assume that the struts are sequentially extruded following an Euler path that expands radially outward from the center of the gridshell, as described in our previous work.[14] With these assumptions, Fig. 13 plots a trajectory for passive gravity gradient capture for a construction timescale of $\hat{t}_F = 1$ with the gridshell and spacecraft parameters of Table 2. Compared to the 2D trajectories for the triangle unit cell, this trajectory is significantly more complex due to the more elaborate construction sequence and coupled effects between the inertia change and gravity gradient disturbance.

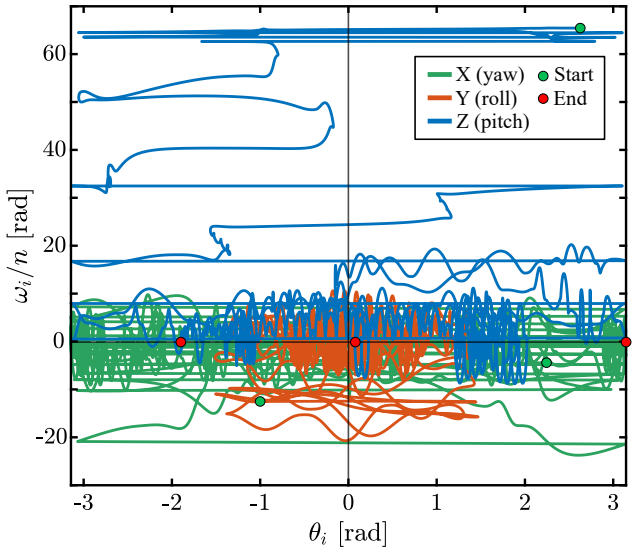

Figure 13: Representative passive trajectory for gravity gradient capture of the 3D curved gridshell.

Parameter	Value
D	20 m
F/D	0.5
L/D	0.1
ρA	0.25 kg/m
s	2 m
m_T	140 kg
m_{SC}	500 kg

Table 2: Gridshell and spacecraft parameters

Initial Condition Sensitivity

Similar to the 2D case, the sensitivity of initial conditions remains of practical importance for passive gravity gradient capture of the curved gridshell. To understand this sensitivity, we use a Monte Carlo analysis with randomized initial conditions applied to the trajectory of Fig. 13. We uniformly and independently perturb the initial orientation and angular velocity within the perturbation radii of $\delta\theta$ and $\delta\hat{\omega}$, respectively, as depicted in Fig. 14. Since uniform sampling of individual Euler angles yields a biased distribution, we sample unit quaternions along a random axis with a uniformly distributed angle $\theta = U(0, \delta\theta)$,[31] and subsequently convert them into Euler angles. We similarly sample angular velocities along a random axis with uniformly distributed norm $||\delta\hat{\boldsymbol{\omega}}||_2 = U(0, \delta\omega)$. With this approach, we integrate the equations of motion forward in time and classify the linear stability of the final state for a total of 5000 randomly sampled perturbations.

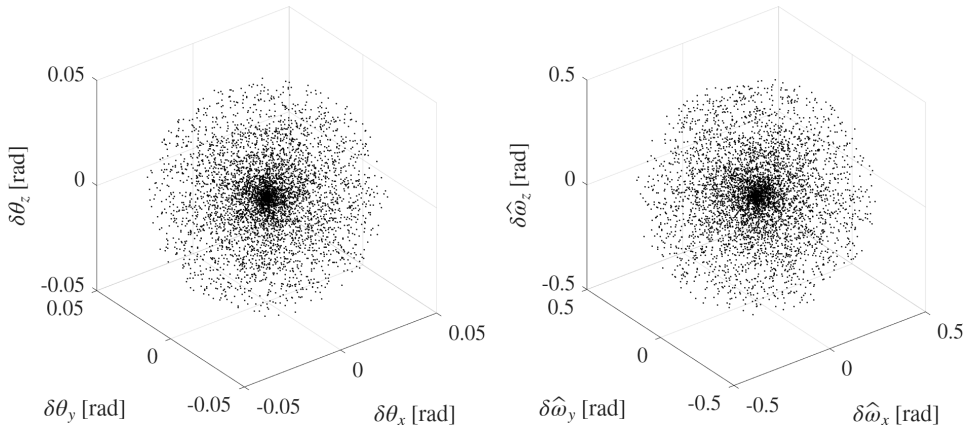

Figure 14: Random perturbations to initial orientation and angular velocity, uniformly sampled within the perturbation radii of $\delta\theta = 0.05$ and $||\delta\hat{\boldsymbol{\omega}}||_2 = 0.5$.

Figure 15 plots the results of the Monte Carlo analysis as slices through the perturbation space. The results show that only certain perturbation directions (e.g., $\delta\theta_y/\delta\theta_x \approx -1$) achieve linearly stable final states. Using the linear stability criterion, the maximum perturbation radii for which 90% of the perturbed initial conditions achieve stable final states are $\delta\theta^* \approx 7.5 \times 10^{-3}$ rad and $||\delta\hat{\boldsymbol{\omega}}||_2^* \approx 0.05$ rad. These values are computed by plotting a histogram of the sampled perturbations and estimating the critical radii at which 90% of them satisfy linear stability at the final state. Due to the normalization of the angular velocity with the orbit angular velocity, the angular velocity sensitivity increases for higher orbit altitudes. For example, in LEO ($n = 10^{-3}$ rad/s), the critical perturbation radius is $||\delta\boldsymbol{\omega}||_2^* \approx 10$ arcsecond/s, but it decreases to $||\delta\boldsymbol{\omega}||_2^* \approx 0.6$ arcsecond/s in GEO ($n = 7 \times 10^{-5}$ rad/s). These are stringent pointing requirements to achieve with modern attitude determination and control systems.[32] Additionally, the high initial angular velocity required for the trajectory in Fig. 13 may not be compatible with the angular rate requirements on sensitive instruments and sensors such as star trackers.

Decreased Initial Condition Sensitivity with Gravity Gradient Boom

An approach to decrease the initial condition sensitivity for passive gravity gradient capture is to deploy a boom along the orbit radius vector before starting the construction process. Intuitively, the additional boom inertia helps stabilize the trajectory by maintaining the minimum principal inertia axis along the orbit radius vector. As an example, consider a gravity gradient boom deployed along the gridshell axis (Fig. 16) such that the final stable orientation consists of the gridshell facing either toward or away from Earth. The required boom length L_B and tip mass m_b to maintain this stable orientation satisfy the inertia inequality $I_{xx} \leq I_{yy} \leq I_{zz}$. We can estimate the required boom length by modeling the boom as a slender rod with linear density $(\rho A)_B$ and the gridshell as a circular plate of diameter D with height h and mass m_T, as

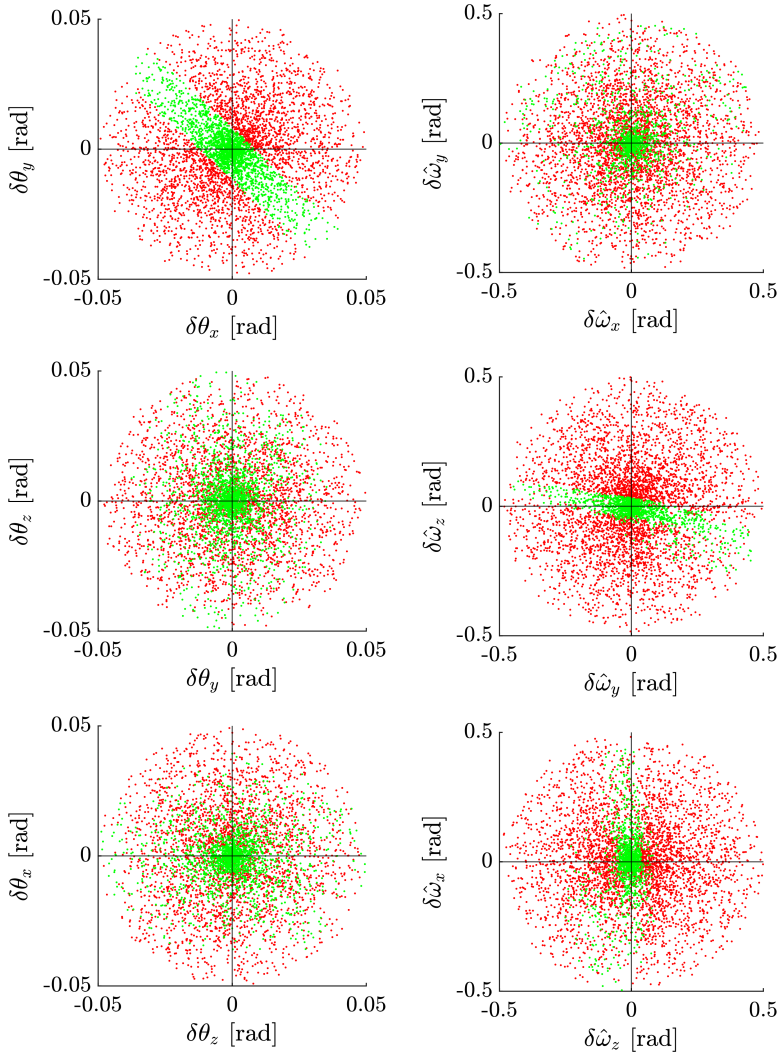

Figure 15: Stability of passive gravity gradient capture due to perturbations to initial conditions. Green dots represent perturbations that result in stable final states, whereas red dots result in unstable final states.

follows:[14]

$$h = \frac{D^2}{16F}, \tag{28}$$

$$m_T = \frac{\pi\sqrt{3}\rho A D^2}{2L}. \tag{29}$$

Using the parameters in Table 2, Fig. 17 plots the minimum boom length L_B as a function of the gridshell geometry for a boom with a constant tip mass $m_b = 50$ kg and a boom density equivalent to the strut density, i.e., $(\rho A)_B = \rho A$. The minimum boom length scales with the mass of the truss, i.e., quadratically with diameter and inversely with strut length (Eq. 29).

To understand the effect of the boom on the trajectories for passive gravity gradient capture, we integrate the equations of motion backwards in time from the final configuration with the additional inertia of the boom. Figure 18 plots a representative trajectory for the gridshell and spacecraft parameters of Table 2 after the initial deployment of a boom of length $L_B = 50$ m, tip mass $m_T = 50$ kg, and boom density equivalent to

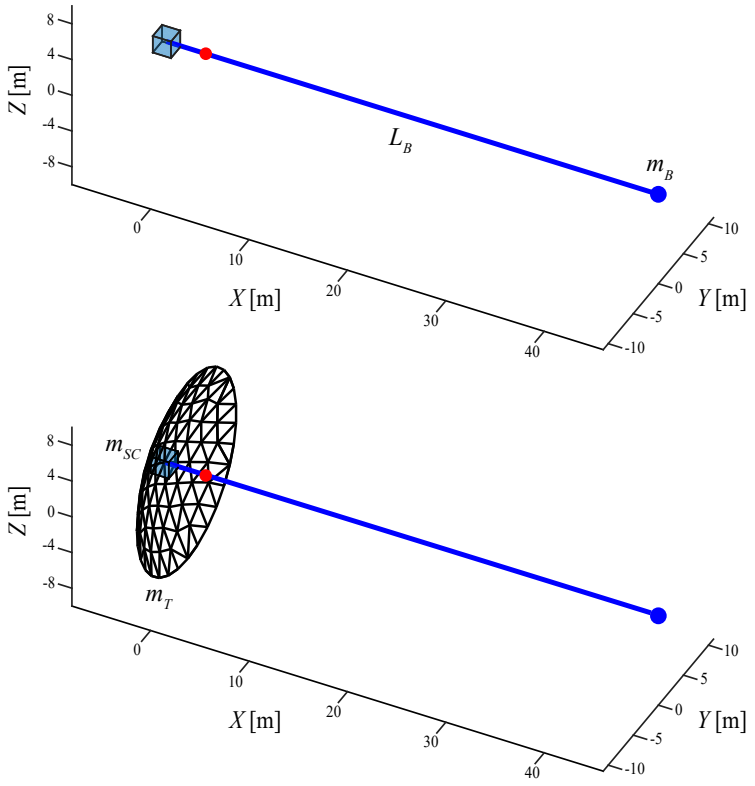

Figure 16: Deployment of a gravity gradient boom followed by construction of the curved gridshell.

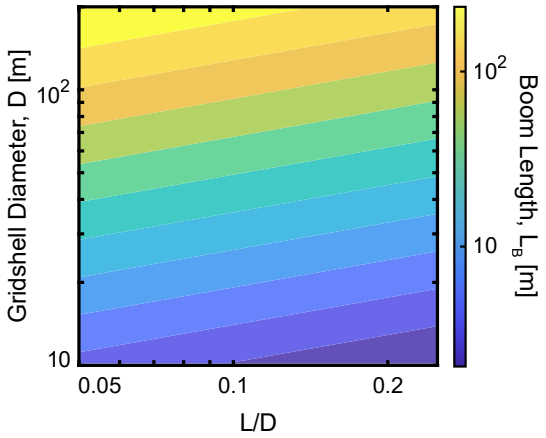

Figure 17: Minimum required boom length L_B as a function of gridshell geometry.

the strut density, i.e., $(\rho A)_B = \rho A$. The results indicate that the trajectory has an initial angular velocity with a norm four times smaller than the trajectory without the boom (Fig. 13). In addition, the results of a Monte Carlo analysis analogous to the previous subsection with 5000 randomly sampled perturbations suggest that the boom significantly reduces the sensitivities to initial orientation and angular velocity perturbations. The Monte Carlo estimates of the maximum perturbation radii ($\delta\theta^* \approx 0.06$ rad and $||\delta\hat{\boldsymbol{\omega}}||_2^* \approx 1.05$ rad) are an order of magnitude larger than the maximum perturbation radii sans boom. Thus, a gravity gradient boom can significantly reduce the initial condition sensitivity of trajectories for passive gravity gradient capture.

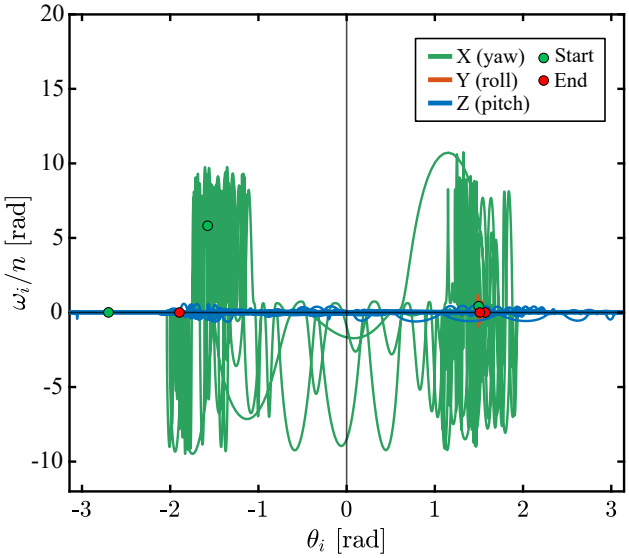

Figure 18: Representative passive trajectory for gravity gradient capture of the 3D curved gridshell after deployment of a gravity gradient boom.

CONCLUSION

This paper has explored the combined effects of mass property changes and gravity gradient disturbances on the attitude dynamics of spacecraft during in-space assembly and manufacturing (ISAM). A scaling analysis determined that the gravity gradient torque is the dominant disturbance torque on ISAM spacecraft in low Earth orbit. Motivated by this analysis, a passive approach to attitude control during ISAM was proposed that exploits gravity gradients to achieve a stable orientation at the end of an ISAM process. The feasibility of this approach, referred to as passive gravity gradient capture, was established via case studies on the construction of a 2D triangle unit cell and a 3D curved gridshell. Subsequent analyses demonstrated that the initial conditions for passive gravity gradient capture were highly sensitive to perturbations. In an effort to reduce this initial condition sensitivity, a gravity gradient boom was deployed before the start of the construction of a curved gridshell. For this specific example, the gravity gradient boom reduced the sensitivity of initial conditions by an order of magnitude. More generally, designing an ISAM process to maintain the minimum principal inertia axis in the direction of the orbit radius vector can facilitate the robust passive gravity gradient capture of large space structures.

ACKNOWLEDGEMENTS

H.G.B acknowledges insightful discussions with Prof. Jack Wisdom of MIT regarding time reversibility, and financial support from the NASA Space Technology Graduate Research Opportunities (NSTGRO) program, through Grant No. 80NSSC23K1195.

REFERENCES

[1] N. N. Lee, J. W. Burdick, P. Backes, S. Pellegrino, K. Hogstrom, C. Fuller, B. Kennedy, J. Kim, R. Mukherjee, C. Seubert, and Y.-H. Wu, "Architecture for in-space robotic assembly of a modular space telescope," *Journal of Astronomical Telescopes, Instruments, and Systems*, Vol. 2, No. 4, 2016, p. 041207, https://doi.org/10.1117/1.JATIS.2.4.041207.

[2] M. W. Thomson, "The AstroMesh Deployable Reflector," *IEEE Antennas and Propagation Society International Symposium*, Vol. 3, Orlando, Florida, 1999, pp. 1516–1519, https://doi.org/10.1109/APS.1999.838231.

[3] J. C. Mankins, "A Technical Overview of the "SunTower" Solar Power Satellite Concept," *Acta Astronautica*, Vol. 50, No. 6, 2002, pp. 369–377, https://doi.org/10.1016/S0094-5765(01)00167-9.

[4] J. A. Banik, "Realizing Large Structures in Space," *Proceedings of 2015 US Frontiers of Engineering*, 2016, pp. 55–62.

[5] J.-E. Suh, S. P. Dassanayake, M. W. Thomson, and S. Pellegrino, "Scaling Laws for Deployable Mesh Reflector Antennas," *AIAA Journal*, Vol. 62, No. 10, 2024, pp. 3948–3959, https://doi.org/10.2514/1.J063940.

[6] B. Jenett and K. Cheung, "BILL-E: Robotic Platform for Locomotion and Manipulation of Lightweight Space Structures," *25th AIAA/AHS Adaptive Structures Conference*, Grapevine, Texas, 2017. AIAA 2017-1876, https://doi.org/10.2514/6.2017-1876.

[7] W. Doggett, J. Dorsey, T. Jones, M. Mikulas, J. Teter, and D. Paddock, "TriTruss: A New and Novel Structural Concept Enabling Modular Space Telescopes and Space Platforms," *International Astronautical Congress*, Washington, D.C., 2019. NF1676L-32522.

[8] J.-E. Suh, S. P. Dassanayake, M. Thomson, and S. Pellegrino, "Scalable Concept for Reflector Antenna Assembled in Space," *AIAA Scitech Forum*, Orlando, Florida, 2024. AIAA 2024-0823, https://doi.org/10.2514/6.2024-0823.

[9] B. Levedahl, R. P. Hoyt, T. Silagy, J. Gorges, N. Britton, and J. Slostad, "Trusselator™ technology for in-situ fabrication of solar array support structures," *AIAA Scitech Forum*, Kissimmee, Florida, 2018. AIAA 2018-2203, https://doi.org/10.2514/6.2018-2203.

[10] A. Aulicino, J. A. Sorensen, T. W. Murphey, D. J. Hunt, and M. Folkers, "Structural Testing of an ISAM Truss Architecture for Large Space Structures," *AIAA Aviation Forum and ASCEND*, Las Vegas, Nevada, 2024. AIAA 2024-4936, https://doi.org/10.2514/6.2024-4936.

[11] N. S. Hmeidat, M. Zakoworotny, Y. S. Kim, T. B. Le, G. DeBrun, R. Shah, J. J. Lessard, J. S. Moore, J. W. Baur, P. H. Geubelle, N. R. Sottos, and S. H. Tawfick, "Reactive Extrusion of Frontally Polymerizing Continuous Carbon Fiber Reinforced Polymer Composites," *Composites Part A: Applied Science and Manufacturing*, Vol. 190, 2025, p. 108609, https://doi.org/10.1016/j.compositesa.2024.108609.

[12] H. G. Bhundiya and Z. C. Cordero, "Bend-Forming: A CNC Deformation Process for Fabricating 3D Wireframe Structures," *Additive Manufacturing Letters*, Vol. 6, 2023, p. 100146, https://doi.org/10.1016/j.addlet.2023.100146.

[13] P. C. Hughes, *Spacecraft Attitude Dynamics*. Courier Corporation, 2012.

[14] H. G. Bhundiya, M. A. Marshall, and Z. C. Cordero, "Fabrication Time Diagrams for In-Space Manufacturing of Large Reticulated Structures," *Journal of Manufacturing Science and Engineering*, Vol. 146, No. 12, 2024, p. 121004, https://doi.org/10.1115/1.4066721.

[15] R. B. Kershner and R. E. Fischell, "Gravity-Gradient Stabilization of Earth Satellites," *IFAC Proceedings Volumes*, Vol. 2, No. 1, 1965, pp. 249–266, https://doi.org/10.1016/S1474-6670(17)69092-X.

[16] S. H. Siegel and N. S. Vishwanath, "Analysis of the Passive Stabilization of the Long Duration Exposure Facility," Tech. Rep. NASA-CR-159023, NASA Langley Research Center, Hampton, Virginia, 1977.

[17] R. R. Kumar, M. L. Heck, and B. P. Robertson, "Predicted Torque Equilibrium Attitude Utilization for Space Station Attitude Control," *Guidance, Navigation and Control Conference*, Portland, Oregon, 1990. AIAA-90-3318-CP, https://doi.org/10.2514/6.1990-3318.

[18] N. S. Bedrossian, S. Bhatt, W. Kang, and I. M. Ross, "Zero-Propellant Maneuver Guidance," *IEEE Control Systems Magazine*, Vol. 29, No. 5, 2009, pp. 53–73, https://doi.org/10.1109/MCS.2009.934089.

[19] E. J. Bowers Jr. and C. E. Williams, "Optimization of RAE satellite boom deployment timing," *Journal of Spacecraft and Rockets*, Vol. 7, No. 9, 1970, pp. 1057–1062, https://doi.org/10.2514/3.30102.

[20] R. D. Werking, R. Berg, K. Brokke, T. Hattox, G. Lerner, D. Stewart, and R. Williams, "Radio Astronomy Explorer-B Post-Launch Attitude Operations Analysis," Tech. Rep. NASA-TM-X-70728, NASA Goddard Space Flight Center, Greenbelt, Maryland, 1974.

[21] D. L. Blanchard, "Flight Results from the Gravity-Gradient-Controlled RAE-1 Satellite," *Astrodynamics Conference*, Williamsburg, Virginia, 1986. AIAA 86-2140, https://doi.org/10.2514/6.1986-2140.

[22] J. A. Atchison and M. A. Peck, "Length Scaling in Spacecraft Dynamics," *Journal of Guidance, Control, and Dynamics*, Vol. 34, No. 1, 2011, pp. 231–246, https://doi.org/10.2514/1.49383.

[23] J. E. Hurtado, "Analytical Dynamics of Variable-Mass Systems," *Journal of Guidance, Control, and Dynamics*, Vol. 41, No. 3, 2018, pp. 701–709, https://doi.org/10.2514/1.G002917.

[24] J. Solá, "Quaternion kinematics for the error-state Kalman filter," arXiv:1711.02508, 2017, https://doi.org/10.48550/arXiv.1711.02508.

[25] F. O. Eke and T. C. Mao, "On the Dynamics of Variable Mass Systems," *International Journal of Mechanical Engineering Education*, Vol. 30, No. 2, 2002, pp. 123–137, https://doi.org/10.7227/IJMEE.30.2.4.

[26] H. Schaub and J. L. Junkins, *Analytical Mechanics of Space Systems*. AIAA, 2003.

[27] S. H. Strogatz, *Nonlinear Dynamics and Chaos*. Chapman and Hall/CRC, 2024.

[28] J. A. Beck and C. D. Hall, "Relative Equilibria of a Rigid Satellite in a Circular Keplerian Orbit," *The Journal of the Astronautical Sciences*, Vol. 46, 1998, pp. 215–247, https://doi.org/10.1007/BF03546235.

[29] G. J. Sussman and J. Wisdom, *Structure and Interpretation of Classical Mechanics*. The MIT Press, 2015.

[30] J. M. Hedgepeth, "Critical requirements for the design of large space structures," *2nd AIAA Conference on Large Space Platforms: Toward Permanent Manned Occupancy in Space*, San Diego, California, 1981. AIAA-81-0443, https://doi.org/10.2514/6.1981-443.

[31] J. J. Kuffner, "Effective Sampling and Distance Metrics for 3D Rigid Body Path Planning," *IEEE International Conference on Robotics and Automation*, Vol. 4, New Orleans, Louisiana, 2004, pp. 3993–3998, https://doi.org/10.1109/ROBOT.2004.1308895.

[32] B. Yost and S. Weston, "State-of-the-Art Small Spacecraft Technology," Tech. Rep. NASA/TP-20240001462, NASA Ames Research Center, Moffett Field, California, 2024.